

THE COMPLEX COOLING CORE OF ABELL 2029: RADIO AND X-RAY INTERACTIONS

T. E. CLARKE, ELIZABETH L. BLANTON¹, AND CRAIG L. SARAZIN

Department of Astronomy, University of Virginia, P. O. Box 3818, Charlottesville, VA 22903-0818, USA

Draft version November 9, 2018

ABSTRACT

We present an analysis of *Chandra* observations of the central regions of the cooling flow cluster Abell 2029. We find a number of X-ray filaments in the central 40 kpc, some of which appear to be associated with the currently active central radio galaxy. The outer southern lobe of the steep-spectrum radio source appears to be surrounded by a region of cool gas and is at least partially surrounded by a bright X-ray rim similar to that seen around radio sources in the cores of other cooling flow clusters. Spectroscopic fits show that the overall cluster emission is best fitted by either a two temperature gas ($kT_{high} = 7.47$ keV, $kT_{low} = 0.11$ keV), or a cooling flow model with gas cooling over the same temperature range. This large range of temperatures (over a factor of 50) is relatively unique to Abell 2029 and may suggest that this system is a very young cooling flow where the gas has only recently started cooling to low temperatures. The cooling flow model gives a mass deposition rate of $\dot{M} = 56^{+16}_{-21} M_{\odot} \text{ yr}^{-1}$. In general, the cluster emission is elongated along a position angle of 22° with an ellipticity of 0.26. The distribution of the X-ray emission in the central region of the cluster is asymmetric, however, with excess emission to the north-east and south-east compared to the south-west and north-west, respectively. Fitting and subtracting a smooth elliptical model from the X-ray data reveals a dipolar spiral excess extending in a clockwise direction from the cluster core to radii of ~ 150 kpc. We estimate a total mass of $M_{spiral} \sim 6 \times 10^{12} M_{\odot}$ in the spiral excess. The most likely origins of the excess are either stripping of gas from a galaxy group or bare dark matter potential which has fallen into the cluster, or sloshing motions in the cluster core induced by a past merger.

Subject headings: cooling flows — galaxies: clusters: general — galaxies: clusters: individual (Abell 2029) — intergalactic medium — radio continuum: galaxies — X-rays: galaxies: clusters

1. INTRODUCTION

An intracluster medium (ICM) of thermal X-ray gas fills galaxy clusters and traces the structure within the cluster's gravitational potential. In a relaxed system, the thermal gas in outer regions of the cluster has a relatively smooth and symmetric surface brightness distribution, while the inner regions often reveal peaked X-ray emission which is generally interpreted as a cooling flow (Fabian 1994). The thermal gas in the central regions of these cooling flow clusters has a radiative cooling time which is significantly shorter than the Hubble time, leading to mass deposition rates of more than $100 M_{\odot} \text{ yr}^{-1}$ being determined from imaging data from *Einstein* and *ROSAT* (e.g. White et al. 1997; Allen 2000). Analysis of ASCA SIS and GIS data suggested much lower inferred cooling rates (see Makishima et al. 2001, and references therein), and more recently, high-resolution spatially resolved spectral fitting of *Chandra* and *XMM* data have revealed cooling rates that are a factor of a few to ten times lower than those obtained from the imaging analysis (see McNamara 2002, and references therein). Further evidence of lower cooling flow rates comes from observations using XMM's Reflection-Grating Spectrometer which finds no evidence of cool gas in cluster cores below approximately one-third of the ambient cluster temperature (e.g., Peterson et al. 2003).

The cores of cooling flow clusters typically host giant cD galaxies which often contain an excess blue stellar

component, indicating that there is recent star formation in these central regions (McNamara & O'Connell 1989). The cores of these clusters also often contain powerful, steep spectrum radio galaxies. *Chandra* observations of these systems reveal complex surface brightness distributions with X-ray depressions surrounded by bright rims (e.g., Perseus, Fabian et al. 2000; Hydra A, McNamara et al. 2000; Abell 2052, Blanton et al. 2001). The X-ray depressions are frequently filled with radio synchrotron plasma from the lobes of the central radio source. The theoretical models of Heinz et al. (1998) predicted that the expanding radio source would drive shocks into the ICM and heat the surrounding gas. In contrast to this model, X-ray observations reveal that the rims surrounding the depression are composed of cool gas (e.g., Schmidt et al. 2002; Nulsen et al. 2002), although more recent models suggest that the rims may be formed by weak shocks driven by the expanding radio lobes (Reynolds et al. 2001). In addition, X-ray observations of the Perseus cluster by Fabian et al. (2003) may provide evidence of weak shocks or sound waves driven into the ICM by the central radio source. Estimates of the total energy output from the central radio source show that in at least some cases it is sufficient to offset the effects of the cooling flow (e.g., Virgo A, Owen, Eilek, & Kassim 2000; Hydra A, David et al. 2001; Abell 2052, Blanton, Sarazin, & McNamara 2003, Bîrzan et al. 2004).

In this paper we present results of a radio and X-ray analysis of the cooling flow cluster Abell 2029. Abell 2029 is a nearby, $z=0.0767$, Bautz-Morgan type

Electronic address: tclarke@virginia.edu, eblanton@virginia.edu, sarazin@virginia.edu

¹ Chandra Fellow

I, richness class 4.4 (Dressler 1978) cluster of galaxies. Optical observations show that diffuse light from the central cD galaxy (IC 1101) extends over more than 600 kpc (Uson, Boughn, & Kuhn 1991), making it one of the largest known galaxies. The central region of Abell 2029 is host to the steep spectrum radio source PKS 1508+059. The inner regions of the radio galaxy show a compact flat-spectrum core and two oppositely directed jets which undergo roughly 90° bends at distances of $\sim 10 - 15''$ from the core (Taylor et al. 1994). Beyond the bends, Taylor et al. find that the radio emission extends into two steep-spectrum radio tails. The overall source morphology is a C-shaped wide-angle-tailed (WAT) structure that is typical of clusters undergoing mergers (Roettiger, Burns, & Loken 1996), although the source size of 35 kpc is smaller than average for WATs (O’Donoghue, Eilek, & Owen 1990).

The intracluster medium (ICM) in Abell 2029 has been extensively studied in X-rays. On large scales, the X-ray emission from the cluster appears to be very relaxed (Buote & Canizares 1996; Sarazin et al. 1998; Molendi & De Grandi 1999), consistent with the large inferred cooling flow rates of $\dot{M} = 200 - 300 M_\odot \text{ yr}^{-1}$ (Sarazin et al. 1992; Edge et al. 1992; Peres et al. 1998; Sarazin et al. 1998, although see also White 2000; Lewis et al. 2002). Optical observations are somewhat inconsistent with the relaxed cooling-flow picture as they do not reveal any of the typical star-formation indicators such as O II or blue stellar colors in the central cD (McNamara & O’Connell 1989). In this respect, Abell 2029 is nearly unique among clusters with very large inferred cooling rates.

Higher resolution ROSAT HRI observations by Sarazin et al. (1992) of the core reveal a number of X-ray filaments in the central $30''$ (43 kpc). Taylor et al. (1994) find that the radio emission appears to be anti-correlated with the filaments, suggesting that the radio structure traces the low X-ray pressure regions. The presence of the X-ray filaments is still controversial, however, as subsequent analysis of the ROSAT HRI data by White et al. (1994) found no significant evidence of filaments.

Throughout this paper we adopt WMAP cosmological parameters (Bennett et al. 2003) $H_0 = 71 \text{ km s}^{-1} \text{ Mpc}^{-1}$, $\Omega_\Lambda = 0.73$, and $\Omega_m = 0.27$. At the redshift of Abell 2029, this corresponds to a scale of 1.44 kpc/arcsec. The uncertainties quoted in this paper are 90% confidence intervals.

2. OBSERVATIONS AND DATA REDUCTIONS

Abell 2029 was observed with *Chandra* on 2000 April 12 for a total of 19.8 ksec. The observations were taken in Faint (F) mode with the cluster center on the S3 chip which was operating at -120 C . We extracted the archival observations (OBSID 891) and reprocessed the data using CIAO v2.3, and CALDB v2.18 (except where noted otherwise). Only events with *ASCA* grades 0,2,3,4, and 6 were included in the analysis. The back-illuminated S1 CCD chip was used to examine the background during the observations as the cluster emission fills the entire S3 chip. The data were processed using the `lc_clean` script of M. Markevitch to provide consistent comparison with the background files. The data were free of large flares, and we have removed only 128 s of exposure. The period C ACIS blank-sky background

data files included in the *Chandra* Calibration Database² were used in the data analysis.

3. X-RAY IMAGE

The raw *Chandra* image of the entire S3 chip (roughly 860×860 kpc) is shown in Figure 1. This image covers the 0.3 – 10 keV energy band and has not been corrected for exposure or background but has been binned by two pixels. The broad cluster core is visible at the center of the image, and is surrounded by more extended diffuse X-ray emission. The cluster emission is extended in the north-east to south-west direction, and is not distributed symmetrically about the cluster core. In particular, there is a strong decrease in surface brightness ~ 20 kpc to the west of the cluster core and a much more gradual decrease in the other directions. More generally, there appears to be excess emission to the north-east and south-east compared to the south-west and north-west, respectively. This lack of mirror-symmetry has been previously reported from the ROSAT HRI data (Sarazin et al. 1992) and is discussed in more detail in § 6.

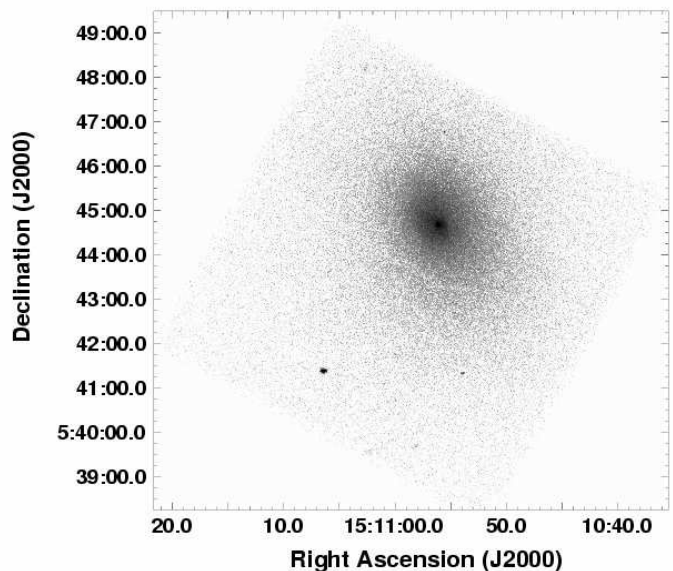


FIG. 1.— Raw *Chandra* image of the full ACIS S3 chip ($\sim 860 \times 860$ kpc) region of Abell 2029 in the 0.3 – 10.0 keV energy band. The image has not been corrected for background or exposure but has been binned by a factor of two. The X-ray emission is elongated in the north-east to south-west direction and shows excess emission to the north-east and south-west of the core compared to the south-west and north-east. The linear negative east-west feature 1.5 below the cluster center is a shadow cast by a foreground spiral galaxy (Clarke et al. 2004).

We have identified individual X-ray sources in the central regions of Abell 2029 using the `wavdetect` algorithm in CIAO (Freeman, Kashyap, Rosner, & Lamb 2002). The significance threshold was set at 10^{-6} which corresponds to roughly 4.7σ , or less than 1 false detection in the S3 field of view. Using the background for each source, we excluded two sources near the detector edges that had a signal-to-noise ratio of less than 3. The final list from the detection algorithm consists of 17 sources. These sources are shown overlaid on the DSS II red im-

² <http://cxc.harvard.edu/caldb/>

age in Figure 2. In the central region of the cluster the algorithm finds both a peak around the cluster-center galaxy IC 1101, and one other peak which appears to be associated with structure in the X-ray filament which traces the radio tail (see § 5). We have compared the source positions to the USNO A2.0 catalog (Monet et al. 1998) and find 7 matches (including IC 1101) for counterparts within $2''$. Four of the optical counterparts fall less than $1''$ from the position of the X-ray peak found by `wavdetect`. Using the Two Micron All Sky Survey catalog (2MASS; Cutri et al. 2001) we find three sources which fall within $1''$ of the X-ray positions. Comparing the offsets of these sources, we find that there is no evidence of a position shift in the X-ray image, thus we have not applied additional astrometry corrections to the X-ray data.

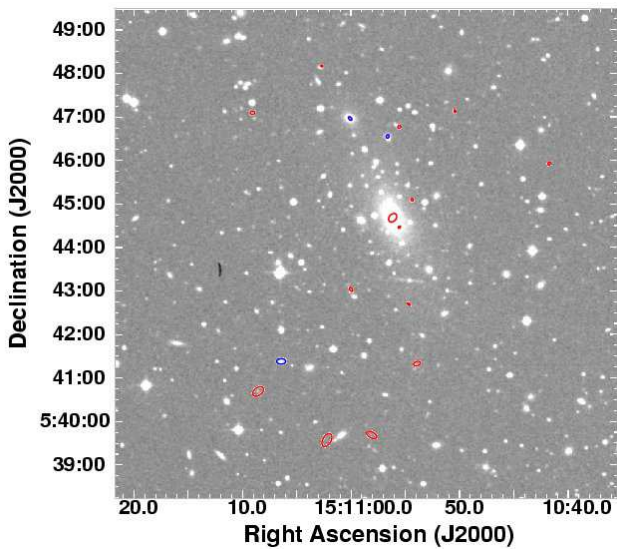


FIG. 2.— DSS II red image of the region covered by the *Chandra* S3 chip. The large object near the center of the image is the cluster-center cD galaxy IC 1101. The linear optical source $1'5$ south of the cD core is the edge-on spiral galaxy which produces photoelectric absorption of the X-ray emission (see Clarke et al. 2004). The X-ray sources identified by `wavdetect` with (without) 2MASS identifications are indicated in blue (red).

Figure 3 shows an adaptively smoothed $0.3 - 10$ keV *Chandra* image of the central $\sim 1'5 \times 1'5$ region of Abell 2029. The adaptive smoothing was done using `csmooth` within CIAO and used a minimum S/N of 3 per smoothing beam. The image has been corrected for background and exposure. This smoothed image shows more clearly the structure in the central regions of Abell 2029. The broad cluster core displays an hourglass shape and there are a number of X-ray enhancements visible as seen in the raw data. On larger scales, the emission is extended in the north-east to south-west direction. The X-ray elongation is similar to that of the diffuse optical halo emission surrounding the central cD. *R*-Band observations by Uson et al. (1991) trace the diffuse light to over 600 kpc from the core along a position angle of 21° east of north. The ellipticity and position angle of the X-ray emission are discussed in more detail in § 6. However, unlike the optical emission, the X-ray image is

clearly asymmetric.

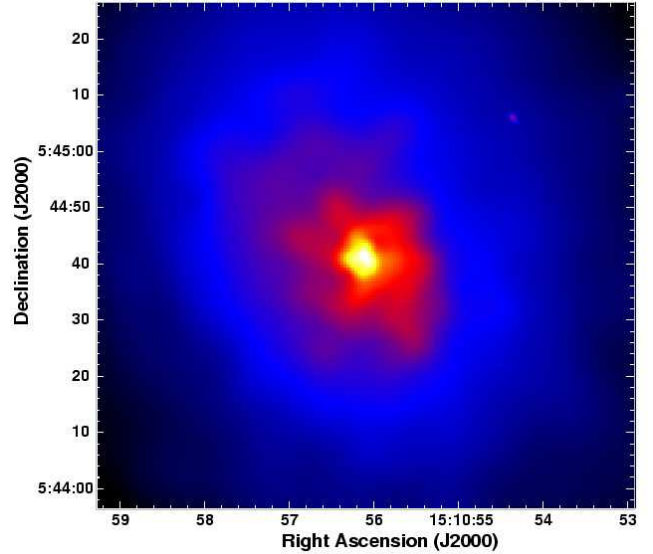


FIG. 3.— Adaptively smoothed X-ray image of the central $\sim 1'5 \times 1'5$ region of Abell 2029 in the $0.3 - 10.0$ keV energy band. The image has been corrected for the effects of background and exposure. The image shows the broad cluster core surrounded by a number of X-ray filaments which extend to the south-east, south-west, north-west, and north-east.

Previous ROSAT HRI images of the inner $30''$ of Abell 2029 showed a number of X-ray filaments running to the north-east, east, south, and south-west (Sarazin et al. 1992). Although the *Chandra* data do not precisely reproduce the locations of the filaments, Figure 3 shows clear X-ray enhancements to the north-east, east, south-west, and north-west of the core. If we just consider the south filament tracing the radio lobe, which we concentrate on in this paper, we find that the counts in a rectangle surrounding the filament are more than 9σ in excess of the average counts in an annulus centered on the core and covering the range of radii of the filament.

4. CLUSTER PROPERTIES

4.1. Integrated X-ray Spectrum of the Cluster Center

Our goal in this section is to obtain the best spectral fit to the integrated spectrum of the cooling flow region of Abell 2029. We begin our analysis with the simplest model (single temperature MEKAL) before proceeding to the more complex models. These spectral fits differ from those of Lewis et al. (2002) who investigated the radial distribution of spectral parameters in concentric annuli, rather than the integrated spectral properties.

The spectral properties of the central region of Abell 2029 were studied using the XSPEC v11.2 software package (Arnaud 1996). The $0.7 - 8.0$ keV spectrum was extracted for a circular region of radius $116''$ (167 kpc), corresponding to the cooling radius found by Sarazin et al. (1992), centered on the cluster core. The extracted region excluded point sources discussed in § 3 but retained the core as no obvious power-law AGN contribution is seen (see § 5.1). The CIAO tool `acisspec` was used to extract the spectrum and produce the weighted response files. The spectrum contained a total of 163,000

background-subtracted counts. We used the more recent CALDB v2.26 under CIAO v3.0.2 for the spectral extraction as it incorporates the best model of the effects of the ACIS QE degradation in the response file. The spectrum was binned in energy using the `grppha` task so that each bin contains at least 25 counts. The blank-sky background files discussed in § 2 were extracted in the same manner over the circular region, excluding the regions around sources detected in the target field. The spectral fits showed significant residuals in the $\sim 1.4\text{--}2.2$ keV energy range that are likely due mainly to the ACIS calibration problems around the Si-K and mirror Ir features, but may also include a contribution from ICM Si and S lines. To exclude the majority of the residuals we would need to exclude this entire energy range. Our fits showed that the addition of a systematic error term of 3% to the data allowed us to retain the majority of the spectral region in the fits. The spectral fits (including the systematic error) were done using both the full 0.7–8.0 keV band (summarized below) and also with the 1.8–2.1 keV region around the mirror Ir edge excluded. We note that fits excluding the 1.4–2.2 keV regions without the addition of a systematic error term are consistent with those presented here. The results of the spectral fitting from both energy ranges are summarized in Table A1.

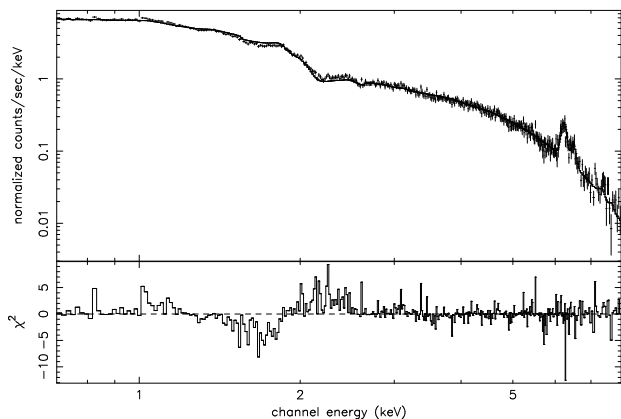


FIG. 4.— Spectrum of the central $116''$ cooling core region. The spectrum is fitted by two MEKAL models with a systematic error term of 3% added to the data. The absorption was fixed to Galactic and the metallicity of the second model was fixed to the (fitted) value of the first model.

Our initial spectral fitting of the central region of Abell 2029 used the single temperature MEKAL plasma emission code (Kaastra & Mewe 1993; Liedahl et al. 1995) to fit the spectrum in the energy range of 0.7–8.0 keV. Fixing the absorption to the Galactic value of $3.14 \times 10^{20} \text{ cm}^{-2}$ as determined from Dickey & Lockman (1990) results in a reduced χ^2 of 1.23, and yields a temperature of $kT = 7.27^{+0.16}_{-0.14}$ keV and an abundance of $Z = 0.47^{+0.03}_{-0.06}$ times solar (assuming metallicity of Anders & Grevesse 1989). Given the relatively poor quality of this fit, we have allowed the absorption to be a free parameter and find that the resulting model is somewhat improved (reduced $\chi^2 = 1.18$), but this fit requires the absorption column to fall below Galactic which may be unlikely. It is more likely that this fit indicates that there is an additional soft X-ray emission component (eg. a second low

temperature thermal component) which is not modeled by a single temperature, and/or the QE degradation correction may not be exact.

The spectral fits are improved (at $> 99.9\%$ level according to the F-test) by adding a second MEKAL component to the model. In this model, the abundances of the two MEKAL components are tied together as there is not enough information in the spectrum to accurately fit them individually. For the two temperature fit with absorption fixed to Galactic, we find a reduced χ^2 of 1.18. The best fitting high and low temperatures are $kT_{\text{high}} = 7.47^{+0.21}_{-0.15}$ keV and $kT_{\text{low}} = 0.11^{+0.07}_{-0.03}$ keV, and the abundance is $Z = 0.49^{+0.03}_{-0.06}$ times solar. The emission measures (MEKAL normalization parameter K) of the hot and cold components are within a factor of about two of each other ($K_{\text{high}} = 5.1 \times 10^{-2} \text{ cm}^{-5}$ and $K_{\text{low}} = 2.1 \times 10^{-2} \text{ cm}^{-5}$). Our metallicity results are in good agreement with Lewis et al. (2002) and the *BeppoSAX* results of Molendi & De Grandi (1999) and Irwin & Bregman (2001). This best-fit two-temperature model is shown in Figure 4. Allowing the absorption to be free results in a model with the same reduced χ^2 , temperatures and abundance to within the 90% confidence errors, and only slightly lower than Galactic absorption of $N_H = 2.22^{+0.92}_{-0.75} \times 10^{20} \text{ cm}^{-2}$. We find that the temperatures of the hot and cool components of the two MEKAL fits differ by more than a factor of 50. One possible explanation for the soft emission component in Abell 2029 is emission from filaments of Warm-Hot Intergalactic Medium surrounding the cluster. Kaastra et al. (2003) have recently studied a sample of 14 clusters using *XMM-Newton* data and find evidence for a spatially extended soft component in the spectrum of five clusters. They find that the emission measure of the soft excess is limited to roughly 10% of that of the hot gas component in the central regions of the clusters but increases significantly to the outer regions of the clusters, where the soft excess becomes dominant in three of the clusters. The small field of view of the ACIS-S3 ccd does not allow us to examine the soft component beyond the central regions of the cluster. We note, however, that the emission measure of the soft component in Abell 2029 is a much larger percentage (roughly 50%) of that of the hot component. This much larger central concentration in Abell 2029 suggests that the emission is not primarily due to intercluster filaments.

We have considered the effects of uncertainties in the *Chandra* calibration and the Galactic absorbing column on the spectral fits since both could have an impact on the fitted soft X-ray component. The observations were taken early in the *Chandra* mission, thus the effects of the QE degradation uncertainty are small. To further limit any uncertainties from calibration problems at low energies we have restricted our spectral analysis to energies above 0.7 keV. In the case of M87, high resolution H I observations showed Galactic columns were roughly 28% lower toward the cluster center (Lieu et al. 1996) than those determined by the lower spatial resolution observations of Stark et al. (1992). We have examined the range of N_H measurements from Dickey & Lockman (1990) in the vicinity of Abell 2029 and find that they vary by at most 12% from the Galactic column used above. Fitting the spectra with a 12% (or even 30%) lower Galactic

column does not change the spectral results within the 90% confidence interval. It is therefore unlikely that the soft emission seen in Abell 2029 is a result of either a calibration error or a variation in the Galactic column.

Given the indications that the cluster has cool gas in the core, and the past high cooling flow rates of $\dot{M} \gtrsim 200 M_{\odot} \text{ yr}^{-1}$ determined for Abell 2029, we have also investigated a cooling flow model for the core. The spectral fits used the MKCFLOW model in conjunction with a MEKAL model such that the high temperature component (kT_{high}) of the cooling flow model is tied to the temperature of the MEKAL model. The MEKAL model represents the hot outer cluster gas along the line of sight. We assume that the cooling flow material cooled from this ambient cluster gas, and thus we fix the abundance in MKCFLOW to that of the MEKAL model for the ambient cluster gas. When the absorption was fixed to Galactic, the MEKAL + MKCFLOW model had best fit high and low temperatures of $kT_{\text{high}} = 7.94^{+0.46}_{-0.23}$ keV and $kT_{\text{low}} = 0.08^{+0.37}_{-0.08}$ keV, an abundance of $Z = 0.50^{+0.03}_{-0.07}$ times solar, and a mass deposition rate of $\dot{M} = 56^{+16}_{-21} M_{\odot} \text{ yr}^{-1}$ (reduced $\chi^2 = 1.19$). Note that the value of kT_{low} is consistent with zero and the best-fit value is well below the lowest photon energies in the spectrum; thus, this fit represents gas which is cooling down to very low temperatures. The data are not sufficient to constrain the MEKAL + MKCFLOW model with the absorbing column, metallicity, kT_{high} , kT_{low} and cooling flow rates free. We have therefore fixed the lower temperature component in the cooling flow model to 0.08 keV based on the results from the MEKAL fits. The subsequent MEKAL + MKCFLOW fits have reduced $\chi^2 = 1.18$, a mass deposition rate of zero and an (unlikely) absorbing column ~ 4 times lower than Galactic. The upper and lower ranges of the temperature distribution spanned by the cooling flow model are consistent with the hot and cool components of the two temperature fits. This cooling flow temperature range of $kT_{\text{high}}/kT_{\text{low}} > 50$ is far greater than seen for other clusters (Peterson et al. 2003), and is discussed further in § 7.

We have also considered an annulus centered on the cluster core running from the cooling radius out to the edge of the S3 chip (i.e. $116''$ to $174''$, or 167 to 251 kpc). We have extracted the spectrum for this region and examined both single and two temperature MEKAL models as well as the MEKAL + MKCFLOW model. The results of these fits are shown in Table A2. As with the cooling radius fits, we find that the two temperature model and the MEKAL + MKCFLOW provide better fits than the single temperature model (i.e. $\chi^2/\text{d.o.f.}_{\text{MEKAL}} = 436/343$, $\chi^2/\text{d.o.f.}_{\text{MEKAL}+\text{MEKAL}} = 399/341$, and $\chi^2/\text{d.o.f.}_{\text{MEKAL}+\text{MKCFLOW}} = 406/341$). The high temperature component from the best fit models in this outer annulus is somewhat higher than that for the cooling core, consistent with the radial temperature increase found by Lewis et al. (2002). The low temperature component remains around 0.1 keV indicating that the cool gas continues to radii of at least 250 kpc from the core of Abell 2029.

The multi-temperature gas and moderate cooling rate we have found for the spectral fits to the *Chandra* data of Abell 2029 are in a possible conflict with the analysis of Lewis et al. (2002) who found no evidence of multi-

phase gas in the cluster. The spectral fits undertaken by Lewis et al. covered the energy range of 0.3 – 8.0 keV but did not include the (then unknown) correction for the QE degradation at soft energies. Without the QE correction, the spectral models would over-predict the flux at low energies thus resulting in weaker constraints on a cool spectral component. The discrepancy between our multi-temperature fits and those of Lewis et al. (2002) are likely due in part to the improved calibration at low energies provided by CALDB v2.26 as well as our restriction to energies above 0.7 keV. We note also that the multiphase and cooling flow models of Lewis et al. (2002) were only applied to each of their inner three annuli which cover radii $< 30''$, while our models were applied to a single region out to the cooling radius of $116''$.

Based on the models we examined, we find that the best fit is produced by the two-temperature MEKAL model where the cluster gas has $kT_{\text{high}} = 7.47$ keV and $kT_{\text{low}} = 0.11$ keV (Table A1). This fit is only slightly better than the MEKAL + MKCFLOW model with absorption fixed to Galactic where we find gas cooling over a range of temperatures between 7.94 keV and 0.08 keV, and a mass deposition rate of $\dot{M} = 56^{+17}_{-21} M_{\odot} \text{ yr}^{-1}$.

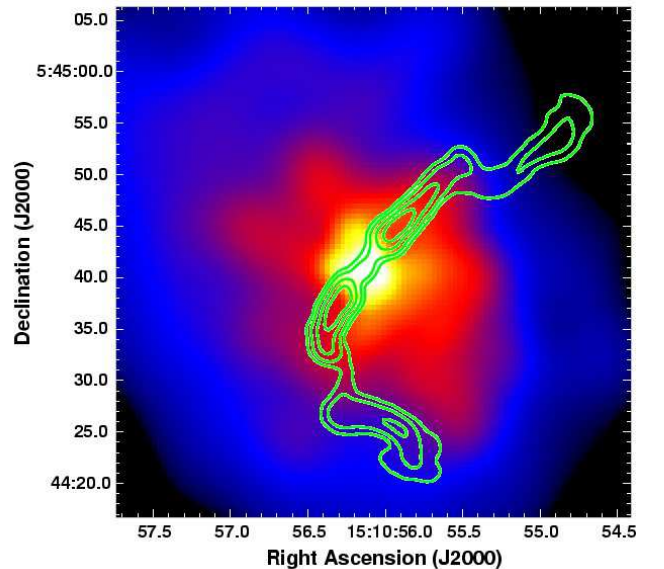


FIG. 5.— The central $50'' \times 50''$ (72×72 kpc) of the adaptively smoothed *Chandra* image shown in Figure 3. The contours show the 1490 MHz radio emission of PKS 1508+059 from Taylor et al. (1994). There are several filaments connected to the currently active radio source: the southern radio lobe is traced by an X-ray filament to the east, and the northern jet is also traced by a filament. There are also several filaments to the north-east which are apparently unrelated to the current radio source.

5. CLUSTER CENTER X-RAY AND RADIO INTERACTION

The central region of Abell 2029 is host to the C-shaped radio source PKS 1508+059. The central radio source has been extensively studied by Taylor et al. (1994). In Figure 5 we show the 1490 MHz radio contours from Taylor et al. overlaid on the central $50''$ region of the adaptively smoothed *Chandra* image. The radio source is composed of two inner jets which extend out to distances of $\sim 10 - 15''$ and two outer tails with sizes of $\sim 20 - 25''$ ($\sim 30 - 35$ kpc). Both radio tails are connected

to the inner radio jets by faint synchrotron bridges. The southern radio tail is bounded to the north by an X-ray filament which traces the full length of the tail. A similar correspondence between the radio and X-ray emission was seen by Taylor et al. when they compared the 1490 MHz radio data to the *ROSAT* HRI image.

The thermal pressure in the X-ray filament was determined by extracting a rectangular region set on the filament and fitting the data within XSPEC. The effect of the overlying ICM was modeled by using a region just exterior to the filament as a local background during the fits. The spectra were binned to 25 counts/bin and were fitted with a single temperature MEKAL model. The absorption was fixed to Galactic, and the abundance was set to $Z = 0.45$ times Solar. The best-fit model ($\chi^2/d.o.f. = 38/40$) gave a temperature of $kT = 4.24^{+2.91}_{-1.43}$ keV, and a normalization of $K = 1.62 \pm 0.20 \times 10^{-4} \text{ cm}^{-5}$, where the normalization is given by

$$K = \frac{10^{-14}}{4\pi D_A^2 (1+z)^2} \int n_H n_e dV. \quad (1)$$

Here, D_A is the angular diameter distance, z is the redshift, n_e and n_H are the electron and hydrogen densities in cm^{-3} , respectively. We assume that the emission is from a prolate cylinder and we find an electron density of $n_e = 0.10 \text{ cm}^{-3}$ and a pressure of $P_{\text{th}} = 1.6 \times 10^{-9} \text{ dyn cm}^{-2}$. Using the same XSPEC model and local background we fitted the emission on either side of the filament and find that the filament is in pressure equilibrium with the ambient thermal gas. The thermal pressure is a factor of 50 larger than the minimum energy synchrotron pressure of $P_{\text{me}} = 2.7 \times 10^{-11} \text{ dyn cm}^{-2}$ as determined by Taylor et al. (1994) and converted to our cosmology. Using the minimum energy parameters from Taylor et al. (1994), the ratio of the energy in the relativistic protons compared to that in electrons (k), to the volume filling factor of relativistic plasma in the radio lobes (η) would have to be $k/\eta \simeq 1.3 \times 10^3$ if no other form of pressure support is present. Similar (although somewhat smaller) discrepancies in pressures are seen in several cooling core systems such as Hydra A (McNamara et al. 2000), Perseus (Fabian et al. 2000), and Abell 2052 (Blanton et al. 2001). These observations suggest that the presence of an additional form of pressure support (such as a hot, thermal component) within the cavities may be necessary for these systems. The isobaric radiative cooling time of the filament is $\tau_{\text{cool}} = 8.4 \times 10^8 \text{ yr}$. This cooling time is significantly shorter than the age of the cluster, but is much longer than the synchrotron age of the radio tail ($\tau_{\text{tail}} = 1.1 \times 10^7 \text{ yr}$) found by Taylor et al. (1994). This suggests that the gas in the X-ray filament did most of its cooling to the current temperature in the dense cluster core and was later displaced to the current position through the influence of the radio source. We determine a mass of the filament of $\sim 1.5 \times 10^{10} M_{\odot}$ which gives a cooling rate in the filament of $\sim 2.5 M_{\odot} \text{ yr}^{-1}$.

At high resolution, the inner regions of the radio source PKS 1508+059 are resolved into a compact core and two bright knots located approximately $1''.3$ on either side of the core. The narrow inner region appears to de-collimate at a distance of $2''$ ($\sim 3 \text{ kpc}$) along each of the oppositely directed radio jets. The location of the

de-collimation is co-incident with a sharp drop in the X-ray surface brightness as seen in Figure 6. The X-ray core appears to have an hour-glass shape with the radio jets propagating along the pinch axis. The sharp X-ray surface brightness drop suggests that the de-collimation of the radio jets is likely due to a decrease in the confining pressure of the surrounding medium. In a study of the flaring of the inner radio jets of 3C 31, Laing & Bridle (2002) find that the radio jets are overpressured by a factor of ~ 8 at the beginning of the flaring region.

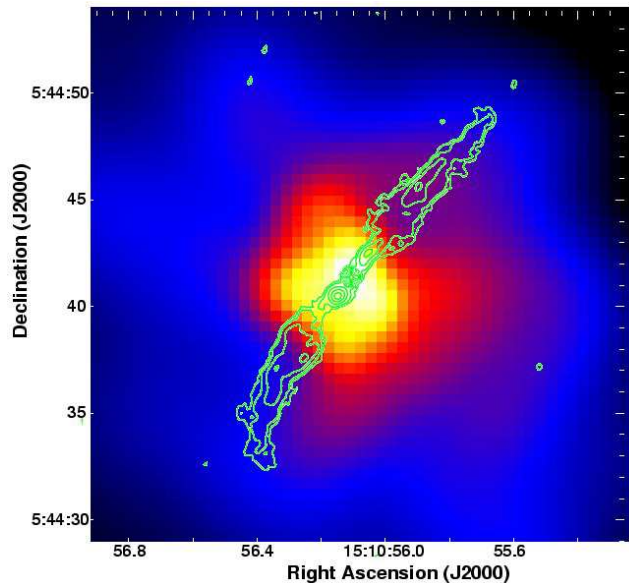


FIG. 6.— The central $25'' \times 25''$ ($36 \times 36 \text{ kpc}$) of the adaptively smoothed *Chandra* image shown in Figure 3. The contours show the 8350 MHz radio emission of PKS 1508+059 from Taylor et al. (1994). The X-ray emission shows the broad hour-glass shaped cluster core. The bright radio core is co-incident with the brightest region of the X-ray core. The radio jets propagate along the pinch axis of the core and are well collimated on either side of the core out to roughly $2''$ ($\sim 3 \text{ kpc}$). Beyond this distance, the radio jets flare outward at the sharp drop in X-ray surface brightness.

Further out, they find that the jets of 3C 31 return to roughly pressure equilibrium with the external medium. An alternative method to de-collimate the jets would be through the interaction of the radio jet with dense gas clumps in the ICM. Unfortunately there is insufficient X-ray data in the jet and de-collimation regions to allow us to determine the pressure and spectral properties in the surrounding thermal medium. We will investigate this connection in more detail with our deep (80 ksec) Cycle 5 *Chandra* data set. Beyond the flaring point, the 8.4 GHz radio jets continue to propagate to a distance of $\sim 10''$ ($\sim 15 \text{ kpc}$). The northern jet appears to follow a linear trajectory, while the tip of the southern jet shows a curvature toward the south. The radio morphology of the southern jet appears to be traced by the cool X-ray filament which extends south of the cluster core (see § 5.2). The radio spectral index ($S_{\nu} \propto \nu^{\alpha}$) of the inner jets of PKS 1508+059 runs from $\alpha = +0.21$ in the core to $\sim \alpha = -2.7$ at the ends of the jets between frequencies of 4860 and 8515 MHz (Taylor et al. 1994). This steepening of the spectrum along the jets is consistent with the confinement of the synchrotron plasma by the external thermal ICM. Taylor et al. (1994) also find that the radio spectrum of the jets shows a curvature such that

the spectral index is steeper at higher frequencies. Using synchrotron aging arguments and the spectral shape of the radio emission, they estimate an age of 9.6×10^5 yr for the inner radio jets, and 1.1×10^7 yr for the outer lobes, where we have converted the lifetimes to our cosmology.

5.1. Is There X-ray Evidence of a Central AGN?

Examination of the raw X-ray data shows that there is no obvious X-ray point source in the core of Abell 2029, however, the presence of the central radio source PKS 1508+059 has led us to search for spectral evidence of the central active galactic nucleus (AGN). The cluster core displays a broad central plateau which has a radius of approximately $6''$. We have extracted the X-ray spectrum from a circular region ($r=3''$, 4.3 kpc) centered on the flat-spectrum radio core (Taylor et al. 1994). We have employed two different techniques to account for the background: 1) a local background determined from an annulus centered on the core with an inner radius of $3''$ and outer radius of $5''$, and 2) a blank-sky background for the circular region determined from the *Chandra* Calibration Database. After background subtraction there were 540 counts in the region centered on the cluster core using the local background file and 1970 counts using the blank-sky background. The data sets were binned to provide at least 25 counts/bin, and a variety of models were examined for each data set. In both cases, the best fit was obtained for a single temperature MEKAL model, and in no case were we able to find a good fit to the core region which included a reasonable power-law component. All fits including a power-law component gave a steep exponent of $\Gamma > 3.4$, while typical radio-loud AGN have $\Gamma \sim 1.5$ (Mushotzky et al. 1993). We note also that there is no obvious point source seen in a hardness ratio map of the broad cluster core. The broad core is consistent with the radial surface brightness profile of the cluster by Lewis et al. (2002). The lack of spectral evidence in the *Chandra* data for a central power-law component suggests that the central AGN may be very weak and/or very heavily obscured.

5.2. Central Temperature Structure

We have created a temperature map of the central region of Abell 2029 to investigate the two-dimensional temperature structure and interactions with the radio source. The map covers the central 95 kpc of Abell 2029 and has compact sources removed. Based on the lack of evidence for excess emission from the central AGN (§ 5.1), we have not excluded data from the cluster core. The temperature map was created within the ISIS software environment (Houck & DeNicola 2000) using an adaptive binning technique. For each pixel in the output map, the spectrum is fit to the smallest surrounding region which contains at least 1050 counts. The smallest extraction region for our temperature map was $3''.5 \times 3''.5$ in the image center, and the largest region was $15''.7 \times 15''.7$ on the image edge. Each spectrum was corrected for a background spectrum extracted from the blank-sky background files from the same source region. The spectra were binned to contain at least 20 counts/bin, and were fitted with a MEKAL model. The absorption was fixed at Galactic, and the abundance was set to $0.45Z_{\odot}$. The resulting temperature map is shown in Figure 7. This map has been convolved with a Gaussian

of width 1.5 pixels to smooth out the inter-pixel variations. The temperatures in the map run from roughly 3.8 keV in the core to ~ 9.5 keV, with the average temperature around 6.8 keV, and typical errors on kT of order 15 – 20%.

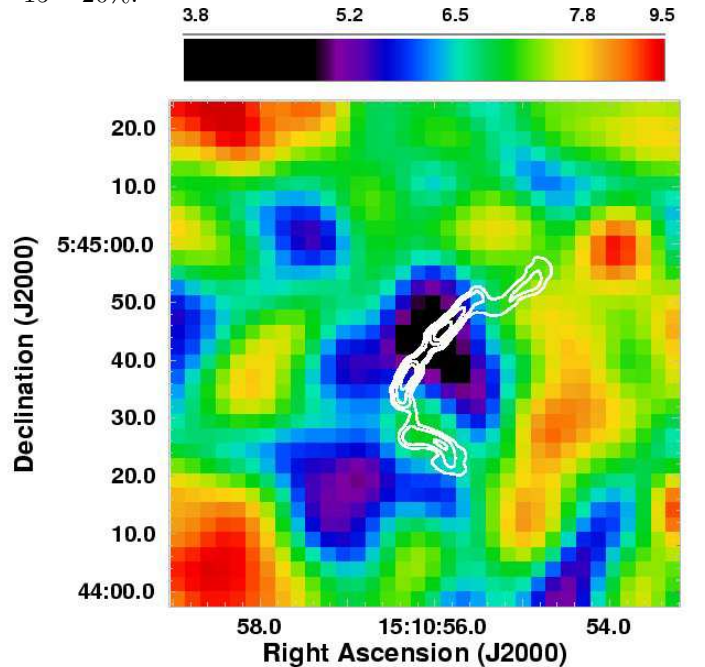


FIG. 7.— Temperature map of the central 95 kpc of Abell 2029 with the color scale shown on top in units of keV. The cluster gas is coolest in the center (around 3.8 keV) and shows cool gas associated with the filament near the southern radio tail. The northern radio tail appears to be embedded in a region of average cluster temperature. The temperature structure in the core of the cluster is complex, likely due to the superposition of the spiral excess feature and the X-ray filaments.

The temperature map shows a triangular-shaped region of cool gas in the cluster core, surrounded by patches of cool and hot gas at larger radii. The central jets of PKS 1508+059 are completely immersed in the cool gas, and the X-ray filament tracing the southern radio tail also appears to be cool. In fact, there is additional cool gas to the south-east of the southern tail, suggesting that it may be surrounded by a cool shell as is found in radio-filled X-ray bubbles (e.g., Nulsen et al. 2002; Fabian et al. 2000; Blanton et al. 2003). There is no evidence in the temperature map of strong X-ray shocks associated with the radio lobes, although we cannot rule out the transfer of energy from the radio source to the thermal gas through weak shocks or pressure waves as seen in Perseus (Fabian et al. 2003). The situation appears to be significantly different for the northern radio extension where the gas surrounding the radio tail is similar to the average cluster temperature. We note, however, that the relation of the gas temperature to the radio structure in the core of Abell 2029 is complicated by the spiral X-ray excess discussed in § 6.

6. SPIRAL EXCESS

In § 3, we mentioned that the diffuse X-ray emission is not symmetrically distributed about the cluster core. In order to investigate this further, we compare the smoothed X-ray image to a smooth elliptical isophotal model. We used a Gaussian smoothed ($\sigma=2''$) im-

age (corrected for background and exposure) as input to the IRAF/STSDAS task `ellipse`. The fits allowed the ellipticity, position angle, and intensity of elliptical isophotes to vary but the ellipse centroids were fixed at the compact X-ray core at RA=15 10 56.11, Dec.= +05 44 41, co-incident with the flat-spectrum radio core of PKS 1508+059 (Taylor et al. 1994). Compact sources were excluded from the fits by setting a clipping threshold to exclude pixels which deviate more than 3σ from the annulus mean. The initial values used for the ellipticity and position angle (PA) were 0.2 and 20° , respectively. The top panel of Figure 8 shows the best-fit ellipticity and position angle for each isophote where the radius of the isophotes follows a geometric progression. The data were fit from a radius of 3 kpc ($\sim 2''$) to the maximum outer semi-major radius of 310 kpc ($3'6$) allowed by the size of the ACIS S3 chip. The PA is roughly constant at 22° from 80 kpc out to 300 kpc, in good agreement with the optical value of 21° determined by Uson et al. (1991). Interior to 80 kpc, the isophotal PA increases to $\sim 44^\circ$ at a distance of 14.5 kpc then drops to 21° at 2.9 kpc, indicating significant structure in the inner regions of the cluster. The ellipticity of the isophotes is fairly constant at 0.26 outside 38 kpc and increases to 0.3 around 34 kpc then drops to 0.07 at 2.9 kpc. In comparison, the diffuse *R*-Band emission of the cD halo has an ellipticity of 0.6 (Uson et al. 1991). A detailed discussion of the intrinsic shape of Abell 2029 based on the observed optical and X-ray ellipticities is presented by Buote & Canizares (1996).

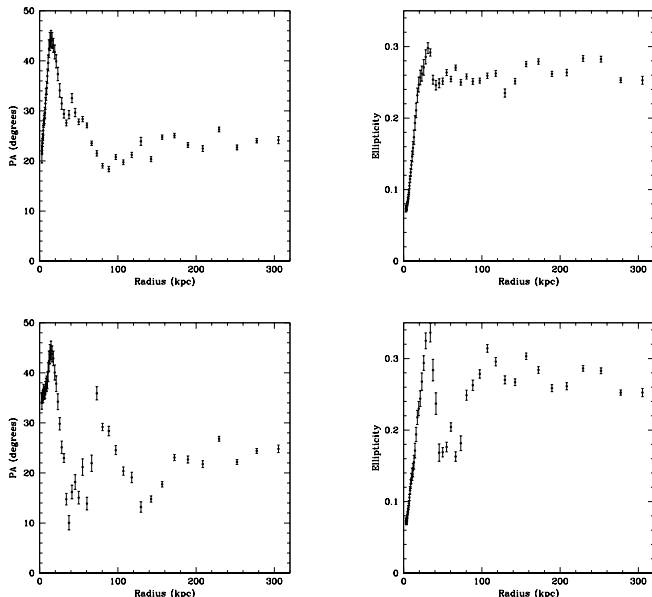


FIG. 8.— Plots of the position angle and ellipticity of the best fit elliptical model to the Gaussian smoothed ($\sigma=2''$) *Chandra* image of the central region of Abell 2029. Top panel shows fits to the full image and bottom panel shows fits after masking the region of excess emission. The PA and ellipticity in the bottom image are more sensitive to features in the X-ray surface brightness due to the smaller averaging areas in each annulus. The spiral galaxy absorption feature (Clarke et al. 2004) is located at a distance of roughly 130 kpc where the bottom panel shows a variation in the PA.

The fit parameters were used to create a smooth elliptical model of the emission which was subsequently sub-

tracted from the Gaussian smoothed X-ray image. The resulting residual image (blanked outside the `ellipse` fitted region) is shown in Figure 9. The residuals show a striking dipolar (i.e., one-armed) spiral pattern which extends from the core in a clockwise direction outward to a position angle (east of north) of roughly 225° and radius of $\sim 1'5 - 2'$. To investigate the possibility of absorption causing the feature, we have split the Gaussian smoothed ($\sigma=2''$) *Chandra* X-ray emission into soft and hard X-ray bands (0.3 – 1.0, and 2.0 – 10.0 keV) and created a hardness ratio image of the central region of the cluster. We do not see any evidence of hard X-ray emission expected from photoelectric absorption near the cluster core. This indicates that the feature is likely due to excess X-ray emission. Figure 9 also clearly reveals the unrelated X-ray absorption $1'5$ south of the cluster core (seen clearly in our hardness ratio image) due to the disk of a foreground edge-on spiral galaxy (Clarke et al. 2004). The positive and negative deviations of the dipolar feature are at the $\sim 15\%$ level compared to the smooth elliptical model, indicating roughly a 30% excess. A morphologically similar spiral X-ray feature is seen in the *Chandra* observations of the Centaurus cluster (Sanders & Fabian 2002). In the case of the *XMM-Newton* observations of Perseus (Churazov, Forman, Jones, & Böhringer 2003), the apparent spiral visible in the surface brightness deviation image is a result of the interaction of the lobes of the central radio source (3C 84) with the dense ICM. This does not appear to be the case for Abell 2029 as the radio lobes are much narrower than those of 3C 84, and the spiral excess extends well beyond the compact radio source.

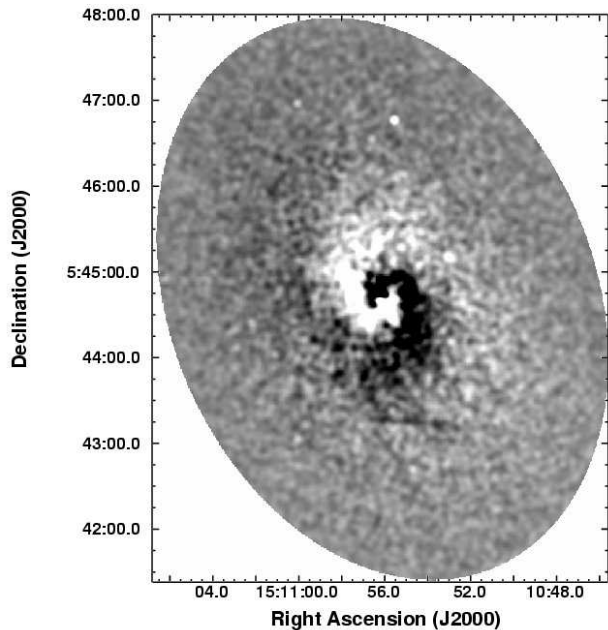


FIG. 9.— Residual image of the central region of A2029 after subtracting a smooth, elliptical isophote model. The model was obtained by fitting the Gaussian smoothed ($\sigma=2''$) image to an elliptical model allowing the ellipticity and position angle to be free in the task `ellipse` in IRAF but with the core position held fixed. The image displays a dipolar spiral pattern. The linear feature $1.5'$ south of the cluster core is due to photoelectric absorption from the disk of a foreground spiral galaxy (Clarke et al. 2004).

We have examined the robustness of the excess emission feature by running a variety of fits to the smoothed X-ray emission with: 1) the centroid, ellipticity and PA free, 2) the centroid and ellipticity fixed and PA free, 3) the centroid and PA fixed and ellipticity free. All fits produced the same excess emission region with only slight variations in the structure in the central region. We have also used the model-subtracted image to create a smooth masked area blocking out the excess emission feature. This mask was then included within the `ellipse` task in IRAF to produce a smooth model of the remainder of the cluster emission. This technique has the advantage of avoiding over-subtraction of the cluster emission due to averaging within annuli that include the excess. The residual image from the masked fitting technique is shown in Figure 10 and the PA and ellipticity are shown in the bottom panel of Figure 8.

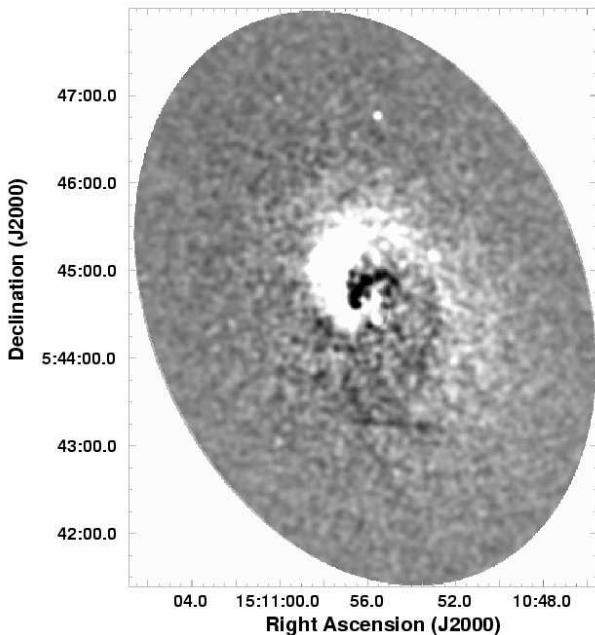


FIG. 10.— Similar residual image to Figure 9 but with the model obtained by masking the region of excess emission in Figure 9 before fitting the elliptical model. This technique reveals the same excess emission structure but reduces the over-subtraction effects seen in the previous image.

To investigate the details of the dipolar spiral feature we have used the positive excess to set an extraction region from the core out to a radius of $\sim 40''$ (58 kpc) at a position angle of 50° . Using CALDB v2.26, we extracted the spectrum of the excess from this region, and also extracted a comparison spectrum by rotating the region mask by 180° about the cluster center. In the energy range of 0.7 – 8.0 keV, the two regions contained 18730, and 14610 background-subtracted counts for the positive and ambient areas, respectively. The data were fit with a single MEKAL model within XSPEC with the absorption fixed to Galactic, and the temperature and abundance left as free parameters. The fit results are shown in Table A3. The region containing the excess is found to be cooler (by ~ 0.9 keV) than the ambient region at the 90% confidence level. Since much of the emission in these two spectra will be due to projected foreground and background gas, it is likely that the real local temperature

contrast is larger than shown in Table A3. In comparison, the plume in the Centaurus cluster is found to be roughly 0.25 keV cooler than the ambient temperature at a similar radius (Sanders & Fabian 2002). In both the Sanders & Fabian (2002) study of Centaurus cluster and our analysis of Abell 2029, the metallicity of the X-ray spiral is found to be consistent with that in the ambient gas.

One possibility for the origin of the spiral excess is that it is a cooler gas cloud which has been stripped as it fell into the center of the cluster. The gas may have been associated with a galaxy or group of galaxies which merged with Abell 2029, or it might have been purely gaseous, or gas occupying a dark matter (DM) potential well. We have estimated the mass of gas required to produce the observed excess. We assumed that the spiral excess region was located in the plane of the sky at the distance of the cluster center. We assumed that the thickness of the spiral excess region along our line-of-sight was equal to the width of the feature in the image (i.e., that it is a spiral tube of excess density). The emissivity was determined from spectral fits to the region. We deprojected the foreground and background emission to obtain the local density in the feature, and integrated this over the volume of the region. The estimated total mass is $M_{\text{spiral}} \sim 6 \times 10^{12} M_\odot$. It is likely that this is a lower limit to the mass required. A quick examination of the *XMM/Newton* archive data on Abell 2029 confirms the existence of this spiral feature, but indicates that it extends about a factor of 2 further out in radius beyond what is seen in the *Chandra* image. The mass in the spiral is increasing rapidly with radius over the range observed with *Chandra*, so this suggests the total mass might be more than a factor of two larger. The mass would also increase if the feature were not located in the plane of the sky. With this gaseous mass, the material could not have come from a single galaxy; it would have to come from a group of galaxies or gas trapped in a dark matter potential well. The mass of the X-ray “plume” seen in the Centaurus cluster was estimated to be more than 1000 times smaller (Sanders & Fabian 2002) and is more likely due to a single infalling galactic system.

In Appendix A, we show that a spiral trajectory is a solution for an object with angular momentum sinking into the center of a cooling flow cluster. This solution applies if the object is sufficiently heavy, has a nonzero angular momentum, and is falling in at the “terminal velocity” (i.e., any initial transients have died away and drag forces nearly balance gravity). In polar coordinates (radius r , angle θ), the orbit is a logarithmic spiral, $r = r_0 \exp[a(\theta - \theta_0)]$ (eqn. A8). A crude fit to the center of the spiral excess in Abell 2029 suggests $\theta_0 = 0$, $r_0 \sim 40''$, and $a \sim -0.4$, if θ is the position angle measured from north to east. The constant a determines the pitch angle of the spiral, and is given by equation (A7). Based on gas density from a deprojection of X-ray surface brightness in the non-spiral-excess region, the required mass column density of the sinking object is $\Sigma \sim 0.01C$ g cm $^{-2}$, where $C \sim 1$ is the drag coefficient of the body. This implies that the total mass of the sinking object is $M_{\text{tot}} \sim 4 \times 10^9 C (D/10 \text{ kpc})^2 M_\odot$, where D is the diameter of the object. For $D \sim 10$ kpc, this mass is much smaller than the gaseous mass needed to produce the spiral excess. The two masses would be similar if $D \geq 100$

kpc, but this is larger than the inner parts of the spiral excess. This suggests that the sinking object was purely gaseous, and was being ablated to produce the spiral as it fell into the cluster center. Unfortunately, this complicates the calculation of the dynamics; clearly, numerical hydrodynamical simulations would be useful to evaluate this model.

Alternatively, the spiral feature might be the result of sloshing motions in the core of the cluster, perhaps induced by a past cluster merger (Maxim Markevitch, private communication). Sloshing features, which are similar to “cold fronts”, have been seen in a number of cooling flow clusters (e.g., Markevitch et al. 2001), but not in the form of extended spirals. A spiral sloshing feature might arise in an offset merger with significant angular momentum. Short spiral features are seen in some merger simulations (e.g., Ricker & Sarazin 2001, Figure 7), but they generally are stronger shocks and occur during very strong mergers. Whether weaker spiral sloshing features can persist long after a merger in an apparently relaxed cluster like Abell 2029 is uncertain; again, numerical hydrodynamical simulations would be useful.

The central radio source PKS 1508+059 reveals a classical C-shaped WAT morphology. As discussed in § 5, the northern radio extension to PKS 1508+059 follows roughly the same position angle as the inner jets, but is offset $\sim 6''$ (8.6 kpc) west of the main jet axis. The outer southern tail is also offset to the west and appears to be rotated by roughly 90° from the inner jet axis. In standard WAT radio sources, this C-shaped morphology is attributed to relative motion between the radio galaxy and the surrounding intergalactic medium. It has been argued that the orbital motions of a cluster-core cD radio galaxy are too small to produce the distortions (Eilek et al. 1984; O’Donoghue et al. 1993). In classical swept-back cluster-core sources, the morphology is therefore often attributed to a merger where the ICM is moving past the radio source (Burns et al. 1994). In Abell 2029, there is no major cluster merger apparent, although we do see the spiral excess which is likely due to either an infalling system or sloshing of the cluster core; thus it is possible that the WAT morphology is due to an interaction between the X-ray gas in the spiral feature and the central radio source. Figure 11 shows the central 95 kpc of the residual image with the 1490 MHz radio contours of Taylor et al. (1994) overlaid. In projection, the excess appears to run directly between the inner southern jet of PKS 1508+059 and the steep-spectrum radio tail. Due to the uncertainties in the origin of the spiral excess, it is difficult to determine if the offset between the inner and outer southern radio structures is due to an interaction of the two features, or if it is simply an unrelated projection effect. The radio tail itself appears to lie in a local depression, with a very compact, deep X-ray depression co-incident with the southern tip of the radio tail. Comparing the 0.3 – 10 keV counts in a circle of radius $2''$ centered on the depression to a surrounding annulus between $2''$ and $12''$ we find that the depression is significant at the 4σ level. Unfortunately, the small number of counts in the depression do not allow us to undertake a more detailed analysis. The northern radio lobe appears to be unaffected by the spiral feature. If the outer radio lobes represent (undisturbed) buoyantly rising bubbles of relativistic particles

and magnetic fields, we would expect them to rise along the lowest thermal pressure gradient (i.e. along the minor axis of the X-ray emission). In this scenario, the most likely source configuration would be an S-shaped source with the northern lobe rising to the north-west and the southern lobe rising to the south-east.

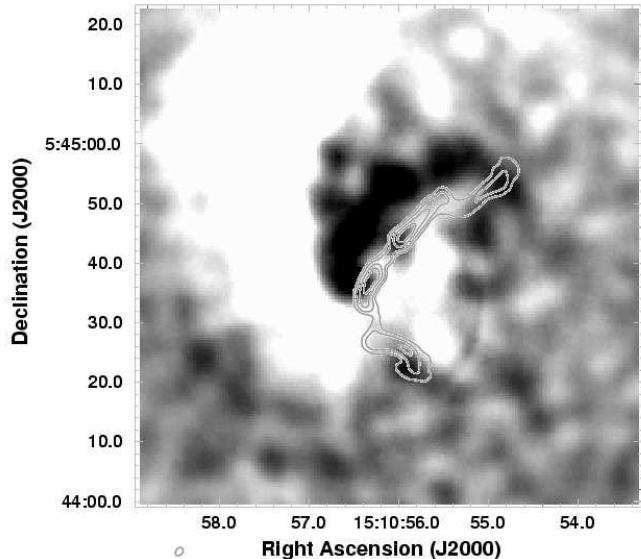


FIG. 11.— Residual image of the central 95 kpc of Figure 10 with VLA 1490 MHz radio data of Taylor et al. (1994) overlaid. The excess emission region runs (in projection) between the southern jet and outer radio lobe.

7. SUMMARY AND DISCUSSION

We have presented a detailed analysis of the *Chandra* ACIS-S3 observations of the central regions Abell 2029. Although this cluster appears to be remarkably relaxed on large scales, there is significant structure within the central 200 kpc radius. In general, the X-ray emission is elliptical along a position angle of 22° , consistent with the position angle of the optical emission of the central cD galaxy. The thermal emission is asymmetric about the cluster core with excess emission to the north-east and south-east compared to the south-west and north-west, respectively. The extent of the excess emission is seen more clearly after we have fitted and subtracted a smooth elliptical model from the data. The resulting X-ray residuals show a clear one-armed spiral pattern running clockwise from the core out to radii of ~ 170 kpc. The excess X-ray emission is $\sim 30\%$ higher than the smooth elliptical model. Based on spectral fits to the region, we estimate a total mass of the spiral excess of $M_{\text{spiral}} \sim 6 \times 10^{12} M_\odot$, although this should be considered a lower limit due to uncertainties in the size and location of the region. It seems likely that the excess feature may be the result of stripping of gas from a galaxy group or gas trapped in a dark matter potential. An alternative possibility is that the excess is the result of sloshing of the cluster core due to a past cluster merger. It would be helpful to have numerical simulations of both models to help assess the feasibility of creating the spiral structure from the different mechanisms.

The central radio source in Abell 2029 displays a wide-angle-tailed morphology which is typical of clusters undergoing mergers. Several authors have previously remarked on the unusual occurrence of such a source in

the core of a relaxed cluster such as Abell 2029 (see e.g. Lewis, Stocke, & Buote 2002; Hardcastle & Sakelliou 2004; Lecavelier des Etangs, Gopal-Krishna, & Durret 2004). One possible explanation for the WAT morphology is that the mechanism responsible for producing the X-ray spiral excess has also influenced the radio source structure. The tip of the southern radio jet of PKS 1508+059 bends toward the south at roughly the location where it intersects (in projection) with the inner regions of the X-ray excess. In addition, the southern radio lobe is displaced (again in projection) to the west of the minor axis of the X-ray emission. If the emission is due to a buoyantly rising detached radio lobe we would expect it to follow the steepest X-ray pressure gradient which should be along the minor axis. In comparison, the northern outer lobe, which is apparently unaffected by the spiral excess, appears to be roughly directed along the minor axis. The southern radio lobe is traced on the western side by a bright X-ray filament which may be a partial shell similar to that seen for Hydra A (McNamara et al. 2000). The temperature map of the central cluster region shows that the gas surrounding the southern radio lobe is cool, consistent with the results found for the bright rims around radio bubbles in clusters such as Perseus (Fabian et al. 2000) and Abell 2052 (Blanton et al. 2001). We will combine the 19 ksec archival data with our deeper 80 ksec Cycle 5 data set to examine the region of the radio foot in more detail to determine if there is a complete rim.

We find that the total cluster spectrum of Abell 2029 is poorly fit by a single temperature thermal model. The best fit is obtained for a two temperature MEKAL model with high and low temperatures of $kT_{high} = 7.47^{+0.21}_{-0.15}$ keV and $kT_{low} = 0.11^{+0.07}_{-0.03}$ keV, and an abundance of $Z = 0.49^{+0.03}_{-0.06} Z_{\odot}$. A nearly identical fit quality is obtained for a cooling flow model with a similar metallicity, gas cooling over a range of temperatures from 7.94 keV down to the limits of the model at 0.08 keV, and a mass deposition rate of $\dot{M} = 56^{+16}_{-21} M_{\odot} \text{ yr}^{-1}$. The range of temperatures from the cooling flow model is more than a factor of 50 between the hot and cool components. This large temperature range is relatively unique as most cooling flow clusters show gas cooling down to only $\sim 1/2 - 1/3$ of the ambient temperature (Peterson et al. 2003). A recent study of the central 20 kpc radius of Abell 2029 with *FUSE* found no evidence of the O VI doublet emission which is a good tracer of gas at $10^5 - 10^6$ K (Lecavelier des Etangs et al. 2004). Based on this non-detection, they place upper limits on the cooling flow rate through 10^6 K of $13 M_{\odot} \text{ yr}^{-1}$. This limit is lower than the $56 M_{\odot} \text{ yr}^{-1}$ we determine to be cooling through $\sim 10^6$ K based on the *Chandra* data. The discrepancy in cooling rates may be largely due to the fact that our cooling rate is determined over a much larger aperture of radius 167 kpc. In a future paper, we will use the deep combined *Chandra* data to investigate the spectral properties in more detail.

Abell 2029 may be a very young cooling core cluster where the gas has only recently started (or re-started) cooling to low temperatures. In this scenario, the radio source may have only recently re-started as a result of feeding from the cooling flow, and thus feedback mechanisms may not have had time to suppress the cooling

to low temperatures. The cooling flow may have only existed for a short time, and too little gas has cooled to low temperatures to produce optical emission lines or star formation. One concern with this feedback scenario is that gas must have cooled and reached the central black hole in order to produce the current radio core. It may be that gas in Abell 2029 is presently cooling for the first time; alternatively, a previous cooling episode may have been disrupted by a merger or heated by the central AGN activity. The presence of the spiral excess feature may suggest that Abell 2029 has had a minor merger in the not too distant past, and numerical simulations by Gómez et al. (2002) indicate that mergers can lead to the disruption of cooling flows in clusters. One argument against a recent merger or hydrodynamical disruption of the core of Abell 2029 is the strong increase in the Fe abundance in the cluster core seen by Lewis et al. (2002). Böhringer et al. (2004) argue that mergers or other processes which disrupt the cooling core might also mix the gas and hence eliminate such abundance gradients. In the case of the minor merger in Abell 2029, the core may not have been significantly disrupted and/or the infalling material may have had an enriched metallicity which could contribute to the observed enhancement. Unfortunately spectral fits to the current data do not provide useful limits on the metallicity of the excess material relative to that of the ambient gas. In addition, it is possible that the onset of cooling was delayed by an AGN heating process which did not mix the cluster-center gas.

Our analysis of the *Chandra* data reveal the presence of significant X-ray structure as well as multiphase gas in the core of Abell 2029. This result is in agreement with previous X-ray studies of the cluster based on *ROSAT* and *ASCA* data (Sarazin et al. 1992; Edge et al. 1992; Peres et al. 1998; Sarazin et al. 1998) but is inconsistent with the conclusions of the *Chandra* analysis of the cluster by Lewis et al. (2002) who found no evidence of multiphase gas or significant X-ray substructure. Lewis et al. (2002) fit the cooling flow model individually to each of the inner three annuli (roughly inner 35 kpc). Unfortunately, at the time of their analysis, the QE degradation of *Chandra* at soft energies was not known, thus their spectral models would over-predict the flux at low energies resulting in weaker constraints on the cool component of the emission. The presence of some X-ray structure in the central region of Abell 2029 was also noted by Lewis et al. (2002): in a Gaussian ($\sigma = 2''$) smoothed image they saw position-angle-dependent variations in the surface brightness within the central $1'$ region where we find the spiral excess feature. Lewis, Buote, & Stocke (2003) used the *Chandra* data to measure the density and temperature distribution in Abell 2029 down to the inner $3''$. Based on the apparent lack of both multiphase gas and significant X-ray structure they used the assumption of hydrostatic equilibrium to determine the distribution of total mass with radius in the system. Fitting the mass profile to various models they found that the distribution was well fit by the Navarro, Frenk, & White (1997) (NFW) profile over the range of radii between 5 and 260 kpc. The lack of deviations of their data from the NFW profile led Lewis et al. (2003) to conclude that the flattened dark matter profile predicted for self-interacting DM (Spergel & Steinhardt 2000) was inconsistent with

the Abell 2029 data. The presence of significant X-ray structure and multiphase gas that we find within the central 130 kpc indicates that the central regions of the cluster are not fully in hydrostatic equilibrium. Without detailed numerical simulations of this system, it is difficult to say at what level the departure from hydrostatic equilibrium has influenced the Lewis et al. (2003) fits to the mass profile.

We thank Greg Taylor for kindly providing us with the calibrated radio data of PKS 1508+059. Maxim Markevitch pointed out the possible relation of the spiral excess with cluster sloshing features, and we are very thankful for his comments. We are grateful to Henrique Schmitt and to Juan Uson for many interesting discussions. The software for temperature mapping was written by John Houck and Joshua Kempner. Support for this work was

provided by the National Aeronautics and Space Administration through *Chandra* awards GO2-3160X and GO4-5149X, issued by the Chandra X-ray Observatory, which is operated by the Smithsonian Astrophysical Observatory for and on behalf of NASA under contract NAS8-39073. Some support was also provided by NASA *XMM/Newton* grant NAG5-13089. Support for E. L. B. was provided by NASA through the *Chandra* Fellowship Program, grant award number PF1-20017, under NASA contract number NAS8-39073. This publication makes use of data products from the Two Micron All Sky Survey, which is a joint project of the University of Massachusetts and the Infrared Processing and Analysis Center/California Institute of Technology, funded by the National Aeronautics and Space Administration and the National Science Foundation.

APPENDIX

SPIRAL SOLUTION FOR SINKING BODY

Here, we derive the equations for the orbit of a sinking body in a cluster of galaxies subject to gas drag and gravity forces. We also present an illustrative solution which has the form of a spiral. We will assume that the cluster is spherical and static. Then, by symmetry, the orbit will be planar. We use the polar coordinates r and θ to describe the orbit, where r is the radius out from the cluster center, and θ is the angle around the orbital plane, measured from any arbitrary axis. Let $\rho(r)$ be the ambient gas density in the cluster. Assume that the mass m and cross-sectional area A of the sinking body are constant. Let \mathbf{v} be the velocity vector of the body. We will write the drag force on the sinking body as $\mathbf{F}_{\text{drag}} = -(1/2) \rho(r) A C(v^2) \mathbf{v}$, where $C(v^2)$ is the drag coefficient C . The speed of the body is given by $v = \sqrt{\dot{r}^2 + (r\dot{\theta})^2}$, where the dots denote time derivatives. Then, the equation for the angular momentum of the sinking body is

$$\frac{d(r^2\dot{\theta})}{dt} = -\frac{1}{2} \frac{\rho(r) C[\dot{r}^2 + (r\dot{\theta})^2]}{\Sigma} \sqrt{\dot{r}^2 + (r\dot{\theta})^2} r^2 \dot{\theta}, \quad (\text{A1})$$

where $\Sigma \equiv m/A$ is the mass column density of the body. Similarly, the equation for the radial acceleration is

$$\ddot{r} - r\dot{\theta}^2 = -\frac{GM(r)}{r^2} - \frac{1}{2} \frac{\rho(r) C[\dot{r}^2 + (r\dot{\theta})^2]}{\Sigma} \sqrt{\dot{r}^2 + (r\dot{\theta})^2} \dot{r}, \quad (\text{A2})$$

where $M(r)$ is the total cluster mass interior to r . We assume that $m \ll M(r)$ at all radii of interest. The second and third terms in equation (A2) are the centrifugal and gravitational accelerations. The final terms in both equations (A1) & (A2) represent the effects of drag.

For our simple illustrative solution, we will assume that the drag coefficient C is constant. We will adopt a singular isothermal sphere model for the mass distribution in the cluster, which implies that $M(r) = 2\sigma^2 r/G$, where σ is the one-dimensional velocity dispersion in the cluster. Since we are mainly interested in the central regions of Abell 2029, which is a cooling core cluster, we adapt a simple form for the intracluster gas density distribution, $\rho(r) = \rho_0(r_0/r)$. This distribution is roughly consistent with the observed gas distributions in the centers of many cooling flow clusters (e.g., White, Jones, & Forman 1997). Here, we will use “0” subscripts to denote the initial position of the sinking body. With these assumptions, the radial and angular equations become

$$\ddot{r} - r\dot{\theta}^2 = -\frac{2\sigma^2}{r} - \frac{1}{2} \frac{\rho_0 r_0 C}{\Sigma} \sqrt{\dot{r}^2 + (r\dot{\theta})^2} \frac{\dot{r}}{r}, \quad (\text{A3})$$

and

$$\frac{d(r^2\dot{\theta})}{dt} = -\frac{1}{2} \frac{\rho_0 r_0 C}{\Sigma} \sqrt{\dot{r}^2 + (r\dot{\theta})^2} r \dot{\theta}. \quad (\text{A4})$$

Any detailed discussion of the full set of solutions to equations (A3) & (A4) is beyond the scope of this observational paper. However, we note that one set of solutions is given by

$$r = r_0 \left(1 + \dot{\theta}_0 a t\right), \quad (\text{A5})$$

and

$$\theta = \frac{1}{a} \ln \left(1 + \dot{\theta}_0 a t\right) + \theta_0. \quad (\text{A6})$$

Here, r_0 and θ_0 are the initial radius and azimuthal angle at $t = 0$, and $\dot{\theta}_0$ is the initial value for the angular velocity. The constant a is given by

$$a \equiv -\frac{\text{sign}(\dot{\theta}_0)}{\sqrt{\left(\frac{2\Sigma}{\rho_0 r_0 C}\right)^2 - 1}}. \quad (\text{A7})$$

The geometric shape of the orbit in this solution is that of a logarithmic spiral,

$$r = r_0 \exp[a(\theta - \theta_0)]. \quad (\text{A8})$$

Equations (A5), (A6), & (A8) do not represent a general solution of the equations. They only apply exactly when the initial radial and angular velocity of the sinking object are given by

$$\dot{r}_0 = -\frac{\sigma \rho_0 r_0 C}{\sqrt{2} \Sigma}, \quad (\text{A9})$$

and

$$\dot{\theta}_0 = \pm \sqrt{\frac{2\sigma^2}{r_0^2} \left[1 - \left(\frac{\rho_0 r_0 C}{2\Sigma} \right)^2 \right]}. \quad (\text{A10})$$

However, one can show that this is an asymptotic (“terminal velocity”) solution for a sinking body with angular momentum which applies after transients associated with the initial conditions have died away. The solution also requires that the mass column of the sinking body exceed a lower limit, $\Sigma > \rho_0 r_0 C/2$. When this limit is approached, the motion becomes radial infall ($\theta = \theta_0 = \text{constant}$) at the terminal velocity for radial motion $r = r_0 - \sqrt{2}\sigma t$. For radial motion, the terminal velocity is $\sqrt{2}\sigma$ under the assumptions made here.

REFERENCES

- Allen, S. W. 2000, MNRAS, 315, 269
Anders, E. & Grevesse, N. 1989, *Geochimica et Cosmochimica Acta*, 53, 197
Arnaud, K. A. 1996, *Astronomical Data Analysis Software and Systems V*, eds. G. Jacoby, and J. Barnes, p. 17, ASP Conf. Series volume 101
Bennett, C. L. et al. 2003, ApJS, 148, 1
Birzan, L., Rafferty, D. A., McNamara, B. R., Wise, M. W., & Nulsen, P. E. J. 2004, ApJ, 607, 800
Blanton, E. L., Sarazin, C. L., McNamara, B. R. 2003, ApJ, 585, 227
Blanton, E. L., Sarazin, C. L., McNamara, B. R., & Clarke, T. E. 2004, ApJ. in press
Blanton, E. L., Sarazin, C. L., McNamara, B. R., & Wise, M. W. 2001, ApJ, 558, L15
Böhringer, H., Matsushita, K., Churazov, E., Finoguenov, A., & Ikebe, Y. 2004, A&A, 416, L21
Buote, D. A. & Canizares, C. R. 1996, ApJ, 457, 565
Burns, J. O., Rhee, G., Owen, F. N., & Pinkney, J. 1994, ApJ, 423, 94
Churazov, E., Forman, W., Jones, C., & Böhringer, H. 2003, ApJ, 590, 225
Clarke, T. E., Uson, J. M., Sarazin, C. L., & Blanton, E. L. 2003, ApJ, 601, 798
Cutri, R. M., et al. 2001, Explanatory Supplement to the 2MASS Second Incremental Data Release, The Two Micron All Sky Survey at IPAC Website: <http://www.ipac.caltech.edu/2mass/releases/second/doc/explsup.htm>
David, L. P., Nulsen, P. E. J., McNamara, B. R., Forman, W., Jones, C., Ponman, T., Robertson, B., & Wise, M. 2001, ApJ, 557, 546
Dickey, J. M., & Lockman, F. J. 1990, ARA&A, 28, 215
Dressler, A. 1978, ApJ, 226, 55
Edge, A. C., Stewart, G. C., & Fabian, A. C. 1992, MNRAS, 258, 177
Eilek, J. A., Burns, J. O., Odea, C. P., & Owen, F. N. 1984, ApJ, 278, 37
Fabian, A. C., et al. 2000, MNRAS, 318, L65
Fabian, A. C., Sanders, J. S., Allen, S. W., Crawford, C. S., Iwasawa, K., Johnstone, R. M., Schmidt, R. W., & Taylor, G. B. 2003, MNRAS, 344, L43
Freeman, P. E., Kashyap, V., Rosner, R., & Lamb, D. Q. 2002, ApJS, 138, 185
Gómez, P. L., Loken, C., Roettiger, K., & Burns, J. O. 2002, ApJ, 569, 122
Hardcastle, M. J., Sakelliou, I. 2004, MNRAS, 349, 560
Heinz, S., Choi, Y., Reynolds, C. S., & Begelman, M. C. 2002, ApJ, 569, L79
Heinz, S., Reynolds, C. S., & Begelman, M. C. 1998, ApJ, 501, 126
Houck, J. C. & DeNicola, L. A. 2000, in ASP Conf. Ser. Vol. 216, *Astronomical Data Analysis Software Systems IX*, ed. N. Manset, C. Veillet, & D. Crabtree (San Francisco: ASP), 591
Irwin, J.A. & Bregman, J.N. 2001, ApJ, 546, 150
Kaastra, J. S., Lieu, R., Tamura, T., Paerels, F. B. S., & den Herder, J. W. 2003, A&A, 397, 445
Kaastra, J. S., & Mewe, R. 1993, A&AS, 97, 443
Laing, R.A., & Bridle, A.H. 2002, MNRAS, 336, 1161
Lecavelier des Etangs, A., Gopal-Krishna, & Durret, F. 2004, A&A, 421, 503
Lewis, A. D., Buote, D. A., Stocke, J. T. 2003, ApJ, 586, 135
Lewis, A. D., Stocke, J. T., & Buote, D. A. 2002, ApJ, 573, L13
Liedahl, D. A., Osterheld, A. L., & Goldstein, W. H. 1995, ApJ, 438, L115
Lieu, R., Mittaz, J. P. D., Bowyer, S., Lockman, F. J., Hwang, C.-Y., & Schmitt, J. H. M. M. 1996, ApJ, 458, L5
Makishima, K., et al. 2001, PASJ, 53, 401
Markevitch, M., Vikhlinin, A., & Mazzotta, P. 2001, ApJ, 562, L153
McNamara, B. R. 2002, in ASP Conf. Ser. Vol. 262, *The High Energy Universe at Sharp Focus: Chandra Science*, ed. E. M. Schlegel & S. D. Vrtilik, (San Francisco: ASP), 351
McNamara, B. R., et al. 2000, ApJ, 534, L135
McNamara, B. R. & O’Connell, R. W. 1989, AJ, 98, 2018
Molendi, S., & De Grandi, S. 1999, A&A, 351, L41
Monet, D. et al. 1998, *The USNO-A2.0 Catalogue*, (U.S. Naval Observatory, Washington, DC)
Mushotzky, R. F., Done, C., & Pounds, K. A. 1993, ARA&A, 31, 717
Navarro, J. F., Frenk, C. S., & White, S. D. M. 1997, ApJ, 490, 493
Nulsen, P. E. J., David, L. P., McNamara, B. R., Jones, C., Forman, W. R., & Wise, M. 2002, ApJ, 568, 163
O’Donoghue, A. A., Eilek, J. A., & Owen, F. N. 1990, ApJS, 72, 75
O’Donoghue, A. A., Eilek, J. A., & Owen, F. N. 1993, ApJ, 408, 428
Owen, F. N., Eilek, J. A., & Kassim, N. E. 2000, ApJ, 543, 611
Peres, C. B., Fabian, A. C., Edge, A. C., Allen, S. W., Johnstone, R. M., & White, D. A. 1998, MNRAS, 298, 416

- Peterson, J. R., Kahn, S. M., Paerels, F. B. S., Kaastra, J. S., Tamura, T., Bleeker, J. A. M., Ferrigno, C., & Jernigan, J. G. 2003, *ApJ*, 590, 207
- Reynolds, C. S., Heinz, S., & Begelman, M. C. 2001, *ApJ*, 549, L179
- Ricker, P. M., & Sarazin, C. L. 2001, *ApJ*, 561, 621
- Roettiger, K., Burns, J. O., & Loken, C. 1996, *ApJ*, 473, 651
- Sanders, J.S., & Fabian, A.C. 2002, *MNRAS*, 331, 273
- Sarazin, C. L., O'Connell, R. W., & McNamara, B. R. 1992, *ApJ*, 389, L59
- Sarazin, C. L., Wise, M. W., & Markevitch, M. L. 1998, *ApJ*, 498, 606
- Schmidt, R. W., Fabian, A. C., & Sanders, J. S. 2002, *MNRAS*, 337, 71
- Spiegel, D. N. & Steinhardt, P. J. 2000, *Phys. Rev. Lett.*, 84, 3760
- Stark, A. A., Gammie, C. F., Wilson, R.W., Bally, J., Linke, R. A., Heiles, C., & Hurwitz, M. 1992, *ApJS*, 79, 77
- Taylor, G. B., Barton, E. J., & Ge, J. P. 1994, *AJ*, 107, 1942
- Uson, J. M., Boughn, S. P., & Kuhn, J. R. 1991, *ApJ*, 369, 46
- White, D. A. 2000, *MNRAS*, 312, 663
- White, D. A., Fabian, A. C., Allen, S. W., Edge, A. C., Crawford, C. S., Johnstone, R. M., Stewart, G. C., & Voges, W. 1994, *MNRAS*, 269, 589
- White, D. A., Jones, C., & Forman, W. 1997, *MNRAS*, 292, 419

TABLE A1. XSPEC FITS TO THE INNER 116'' RADIUS REGION

Model	N_H ($\times 10^{20}$ cm $^{-2}$)	kT_{low} (keV)	kT_{high} (keV)	Abundance (Solar)	\dot{M} (M_{\odot} yr $^{-1}$)	$\chi^2/\text{d.o.f.}$
MEKAL	(3.14)	...	$7.27^{+0.16}_{-0.14}$	$0.47^{+0.03}_{-0.06}$...	532/432=1.23
MEKAL	$1.27^{+0.64}_{-0.43}$...	$7.70^{+0.35}_{-0.13}$	$0.49^{+0.03}_{-0.05}$...	508/431=1.18
MEKAL $_{\text{e}}$	(3.14)	...	$7.24^{+0.12}_{-0.12}$	$0.47^{+0.03}_{-0.05}$...	499/411=1.21
MEKAL $_{\text{e}}$	$0.80^{+0.79}_{-0.27}$...	$7.90^{+0.27}_{-0.17}$	$0.50^{+0.04}_{-0.05}$...	473/410=1.15
MEKAL+MEKAL	(3.14)	$0.11^{+0.07}_{-0.03}$	$7.47^{+0.21}_{-0.15}$	$0.49^{+0.03}_{-0.06}$...	507/430=1.18
MEKAL+MEKAL	$2.22^{+0.92}_{-0.75}$	$0.14^{+0.01}_{-0.03}$	$7.61^{+0.36}_{-0.15}$	$0.50^{+0.02}_{-0.07}$...	506/429=1.18
MEKAL+MEKAL $_{\text{e}}$ ^a	(3.14)	$0.14^{+0.01}_{-0.01}$	$7.47^{+0.23}_{-0.14}$	$0.50^{+0.03}_{-0.07}$...	472/409=1.16
MEKAL+MKCFLOW	(3.14)	$0.08^{+0.37}_{-0.08}$	$7.94^{+0.46}_{-0.23}$	$0.50^{+0.03}_{-0.07}$	56^{+17}_{-21}	513/430=1.19
MEKAL+MKCFLOW	$0.84^{+1.90}_{-0.32}$	(0.08)	$7.83^{+0.26}_{-0.31}$	$0.51^{+0.01}_{-0.05}$	0^{+19}_{-0}	509/430=1.18
MEKAL+MKCFLOW $_{\text{e}}$	(3.14)	$0.08^{+0.35}_{-0.08}$	$8.02^{+0.50}_{-0.18}$	$0.51^{+0.04}_{-0.06}$	62^{+18}_{-21}	477/409=1.17
MEKAL+MKCFLOW $_{\text{e}}$	$0.99^{+0.78}_{-0.52}$	(0.08)	$7.78^{+0.33}_{-0.10}$	$0.51^{+0.01}_{-0.05}$	2^{+9}_{-2}	472/409=1.15

NOTE. — Values in parentheses were held fixed in the models. Models with $_{\text{e}}$ are fit over the 0.7 – 8.0 keV range excluding the 1.8 – 2.1 keV energy interval, while the remainder of the models cover the entire 0.7 – 8.0 keV range.

^aA two temperature MEKAL model with free absorption excluding the 1.8 – 2.1 keV region resulted in an unconstrained temperature on the second component and is not shown here.

TABLE A2. XSPEC FITS TO THE OUTER 116'' < r < 174'' REGION

Model	N_H ($\times 10^{20}$ cm $^{-2}$)	kT_{low} (keV)	kT_{high} (keV)	Abundance (Solar)	\dot{M} (M_{\odot} yr $^{-1}$)	$\chi^2/\text{d.o.f.}$
MEKAL ^a	(3.14)	...	$7.97^{+0.54}_{-0.36}$	$0.34^{+0.08}_{-0.09}$...	436/343=1.27
MEKAL $_{\text{e}}$ ^a	(3.14)	...	$7.92^{+0.54}_{-0.34}$	$0.34^{+0.09}_{-0.08}$...	406/322=1.26
MEKAL+MEKAL	(3.14)	$0.13^{+0.04}_{-0.03}$	$8.71^{+0.57}_{-0.41}$	$0.42^{+0.09}_{-0.11}$...	399/341=1.17
MEKAL+MEKAL	$3.08^{+1.23}_{-0.82}$	$0.14^{+0.02}_{-0.01}$	$8.71^{+0.58}_{-0.39}$	$0.40^{+0.11}_{-0.09}$...	399/340=1.17
MEKAL+MEKAL $_{\text{e}}$	(3.14)	$0.14^{+0.03}_{-0.03}$	$8.71^{+0.57}_{-0.39}$	$0.41^{+0.13}_{-0.09}$...	363/320=1.13
MEKAL+MEKAL $_{\text{e}}$	$0.84^{+1.21}_{-0.84}$	$0.14^{+0.04}_{-0.05}$	$9.29^{+0.74}_{-0.41}$	$0.44^{+0.10}_{-0.11}$...	362/319=1.14
MEKAL+MKCFLOW ^b	(3.14)	$0.09^{+0.30}_{-0.01}$	$10.87^{+1.56}_{-1.30}$	$0.40^{+0.10}_{-0.11}$	27^{+9}_{-8}	406/341=1.19
MEKAL+MKCFLOW $_{\text{e}}$	(3.14)	$0.08^{+0.27}_{-0.08}$	$11.81^{+1.83}_{-1.60}$	$0.41^{+0.12}_{-0.10}$	33^{+7}_{-9}	366/320=1.14
MEKAL+MKCFLOW $_{\text{e}}$	$0.31^{+2.53}_{-0.31}$	$0.08^{+0.76}_{-0.08}$	$10.59^{+1.77}_{-1.03}$	$0.44^{+0.12}_{-0.11}$	12^{+20}_{-7}	362/319=1.13

NOTE. — Values in parentheses were held fixed in the models. Models with $_{\text{e}}$ are fit over the 0.7 – 8.0 keV range excluding the 1.8 – 2.1 keV energy interval, while the remainder of the models cover the entire 0.7 – 8.0 keV range.

^aThe single temperature MEKAL models with free absorption resulted in absorbing columns consistent with zero for both energy range fits and thus they are not shown here.

^bThe MEKAL + MKCFLOW model for the 0.7 – 8.0 keV energy range with free absorption was not able to constrain kT_{low} and is not shown here.

TABLE A3. SPECTRAL FITS TO THE SPIRAL EXCESS FEATURE

Region	kT (keV)	Abundance (Solar)	$\chi^2/\text{d.o.f.}$
Excess	$5.53^{+0.23}_{-0.23}$	$0.65^{+0.12}_{-0.10}$	272/229=1.19
Ambient	$6.41^{+0.39}_{-0.40}$	$0.71^{+0.15}_{-0.14}$	234/207=1.12